ADVANCES IN ATMOSPHERIC SCIENCES, 2025

• **Original Paper** •

Cold Pools Detected by a 356-m Meteorological Tower in a Monsoon Coastal Region※

Chuying MAI[1,2], Yu DU[*1,3,4], Minghua LI[*5], Guixing CHEN[1,3,4], Lin SU[1,3,4], Chao LI[5], Dong FU[1,3,4], and Hoiio KONG[6]

[1]*School of Atmospheric Sciences*, *Sun Yat-sen University*, *and Southern Marine Science and Engineering Guangdong Laboratory (Zhuhai)*, *Zhuhai* 519082, *China*

[2]*Key Laboratory of South China Sea Meteorological Disaster Prevention and Mitigation of Hainan Province*, *China Meteorological Administration*, *Haikou* 570203, *China*

[3]*Guangdong Province Key Laboratory for Climate Change and Natural Disaster Studies*, *Sun Yat-sen University*, *Zhuhai* 519082, *China*

[4]*Key Laboratory of Tropical Atmosphere-Ocean System (Sun Yat-sen University)*, *Ministry of Education*, *Zhuhai* 519082, *China*

[5]*Meteorological Bureau of Shenzhen Municipality*, *and Key Laboratory of Severe Weather in South China*, *Shenzhen* 518040, *China*

[6]*Faculty of Data Science*, *City University of Macau*, *Macau* 999078, *China*

(Received 25 October 2024; revised 17 February 2025; accepted 17 March 2025)

ABSTRACT

Cold pools (CPs) significantly influence coastal heavy rainfall, but detailed observations of them are limited due to the lack of vertical measurement instruments. This study statistically characterizes CPs in the coastal monsoon region of South China using unique data from the 356-m-high Shenzhen Meteorological Tower. CP occurrence correlates with convective activities influenced by the summer monsoon in the seasonal variations and land–sea breeze activities in the diurnal cycle. The CPs predominantly dry the atmosphere, highlighting the dominant role of dry entrainment through convective downdrafts in their formation, with a minor role of hydrometeor evaporation. The average CP depth is estimated at 668.0 m, deeper than tropical CPs but shallower than midlatitude counterparts. The CP properties exhibit diurnal variability, largely influenced by mesoscale convective system (MCS) activities. MCS-induced CPs are deeper and more intense than those from individual convective cells, while linear-MCS-produced CPs are the most intense. These observations from the coastal monsoon region contribute to a comprehensive global understanding of CP characteristics, complementing existing studies from midlatitude and tropical regions.

Key words: cold pool, mesoscale convective system, atmospheric boundary layer, convective-scale processes

Citation: Mai, C. Y., Y. Du, M. H. Li, G. X. Chen, L. Su, C. Li, D. Fu, and H. Kong, 2025: Cold pools detected by a 356-m meteorological tower in a monsoon coastal region. *Adv. Atmos. Sci.*, https://doi.org/10.1007/s00376-025-4446-1.

Article Highlights:

- Cold pool events are associated with convective activities influenced by the summer monsoon and sea breeze activity.
- The wet conditions in monsoon coastal areas lead to reduced evaporation, causing most cold pools to reduce the specific humidity.
- The depths of cold pools in this region are greater than over tropical ocean areas but shallower than over the midlatitude continent.

1. Introduction

Convectively driven cold pools (CPs) play a crucial role in maintaining mesoscale convective systems (MCSs) and producing heavy rainfall. These CPs dynamically interact with the surrounding environment, often triggering new convection. One key process involves the strong gust winds at

※ This paper is a contribution to the special issue on Celebrating the Centennial Anniversary of Sun Yat-sen University and the Tenth Anniversary of Its School of Atmospheric Sciences.

* Corresponding authors: Yu DU, Minghua LI
Emails: duyu7@mail.sysu.edu.cn, 40924641@qq.com

the CP's leading edge uplifting warm ambient air through mechanical lifting (Rotunno et al., 1988). In tropical oceanic regions, moisture rings at the CP edge contain enhanced moisture, providing moist static energy for convection development (Tompkins, 2001; Feng et al., 2015). Mechanical and thermodynamic forcing work synergistically to reduce convective inhibition energy and lift parcels from the surface (Torri et al., 2015).

Given the importance of CPs in weather systems, high-resolution and sophisticated observation techniques are essential to capture their variations across different climate conditions. For instance, de Szoeke et al. (2017) utilized a research vessel to document CP characteristics in the central Indian Ocean, reporting a mean temperature drop of 1.3°C and a decrease in specific humidity of 0.6 g kg^{-1} at the gust front, following a minor humidity increase of 0.25 g kg^{-1} ahead of the front. In contrast, CP signals over midlatitude continents are typically stronger due to greater evaporation in the relatively dry conditions (e.g., Engerer et al., 2008; Joseph et al., 2021; Kirsch et al., 2021). Moisture changes caused by CPs over midlatitude land vary depending on location (e.g., Wakimoto, 1982; van den Heever et al., 2021). Tower measurements in Germany observed that CP passages resulted in sustained increases in moisture (Kirsch et al., 2021), while CPs in the Netherlands are characterized by a dry interior (Kruse et al., 2022).

CP properties influencing convection development are regulated by environmental humidity. Dry atmospheric profiles tend to promote entrainment, resulting in dry downdrafts and subsequent evaporation (Markowski and Richardson, 2010; Böing et al., 2012; Marion and Trapp, 2019). Drager et al. (2020) found that in simulations of continental CPs, moisture rings tend to form on moist surfaces and disappear under dry conditions. When the model's intense rain evaporation exceeds the drying effect of convective downdrafts, moisture rings are simulated over tropical oceans, a phenomenon not typically observed in real-world data (Torri and Kuang, 2016; Chandra et al., 2018).

In monsoonal coastal regions, CP outflows are one of the key local factors contributing to heavy precipitation. They interact with the complex coastal terrain and the moist unstable monsoon flows (Liu et al., 2018; Du et al., 2020; Zhang et al, 2022; Mai et al., 2023; Su et al., 2023). However, due to a lack of measurements, CP characteristics in monsoon coastal regions, which experience humidity conditions distinct from moist oceanic and dry continental regimes, remain underexplored. In West African monsoon regions, CPs during the pre-monsoon period are found to enhance moisture and moist static energy under dry conditions, thereby feeding subsequent convection, whereas they tend to decrease moisture during the monsoon and retreat periods (Garcia-Carreras et al., 2013; Provod et al., 2016).

In South China, a coastal area influenced by the East Asian monsoon, the recently equipped 356-m-high Shenzhen Meteorological Tower (hereinafter referred to as SZMT, Fig. 1) provides a unique opportunity to observe CPs in a monsoonal coastal environment and their vertical structure (Mai et al., 2023). Using this unique resource, this study aims to compile a comprehensive statistical database of CP observations in coastal monsoon areas. By adopting a methodology similar to that used in Germany (Kirsch et al., 2021), this study enables direct comparisons with results from midlatitude continental regimes, thereby contributing to a more complete global understanding. Additionally, the study investigates CP variability in relation to various parent convection modes, aiming to better understand the complex rain–CP–rain relationship. These findings are expected to provide new insights into CP processes and coastal rainfall, offer observational support for high-resolution simulations, and ultimately aid in improving predictions of heavy rainfall in global monsoonal coastal areas. Following this introduction, section 2 presents the observational data and CP identification methodology, section 3 describes the CP features, and section 4 provides a summary and discussion.

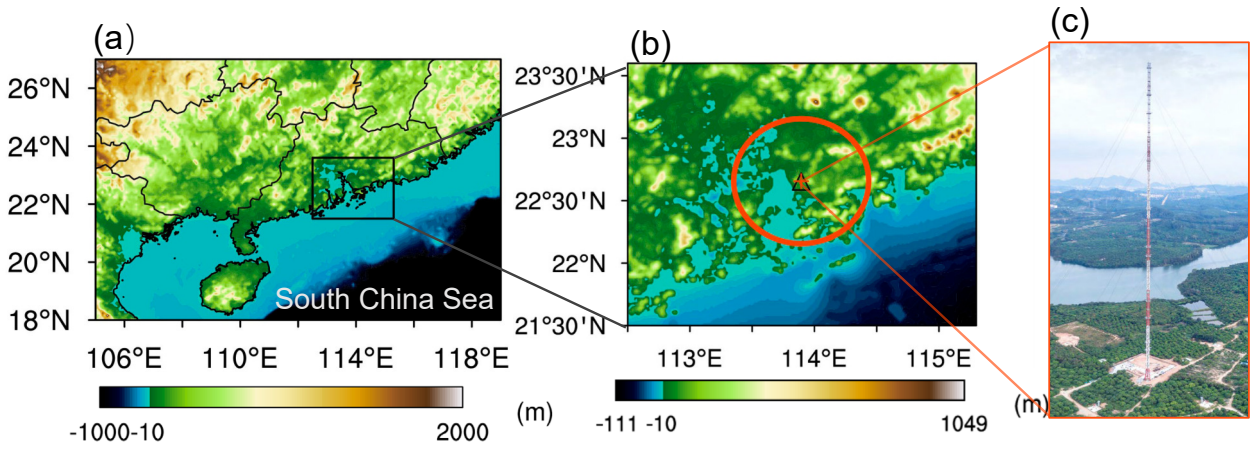

Fig. 1. (a, b) Terrain and bathymetry (units: m) near the observation instruments and their locations. The red cross, black triangle, and red circle in (b) denote the locations of SZMT, G3502, and a range within a radius of 55 km from SZMT, respectively. (c) Photograph of SZMT.

2. Data and methods

2.1. *Observational data*

Observational data spanning 2018–20 utilized in this study are derived from the 356-m-high SZMT, located on the coast of South China (22.66°N, 113.89°E, Fig. 1). SZMT records meteorological variables, including temperature, horizontal wind, and relative humidity, at 13 measurement levels: 10, 20, 40, 50, 80, 100, 150, 160, 200, 250, 300, 320, and 350 m. Pressure data are available at 50, 100, and 300 m. The data have a temporal resolution of 5 min, which is sufficient to capture atmospheric changes during CP activities. To eliminate potential biases from the overestimation of the relative humidity sensor in nearly saturated conditions, a correction method (Mai et al., 2023) is applied to the relative humidity data. Data at the overestimated level is corrected based on the bias between the 2018–20 average and the estimated value obtained from a linear regression of levels (10, 40, 50, 100, 150, 200, and 250 m), which are not overestimated. Specific humidity is estimated using temperature, pressure, and relative humidity as in Mai et al. (2023).

Supplemental precipitation observations are collected from the in situ surface station G3502, located approximately 250 m from SZMT. G3502 provides cumulative precipitation data at 5-min intervals. The precipitation frequency is derived from the occurrences of the 5-min precipitation rate. Radar mosaic images, with a temporal resolution of 6 min, are included to correlate CPs with the convective systems that produce them.

2.2. *Cold pool detection*

To identify the passage of a CP, an objective detection method is employed based on the approach in Kirsch et al. (2021). The method begins by scanning the time series of 10-m temperature for a drop of ⩾ 2 K within a 20-min window. The timing of a CP passing SZMT (t_0) is defined as the first moment when the 10-m temperature decreases by over 0.5 K within the subsequent 5 min. The time series of the subsequent 60 min is considered as the evolution of the part of the same detected CP event. To ensure that the temperature drops are a result of convectively driven CPs, only CPs accompanied by convection (⩾ 35 dBZ) within a radius of 55 km from SZMT during the 2 h preceding their passages are included. Previous studies have shown that CPs typically propagate at a speed ranging from 8 to 15 m s^{-1} (Grant and van den Heever, 2016; Du et al., 2020; Meyer and Haerter, 2020). The chosen radius and time window thresholds ensure that CPs propagating at ~10 m s^{-1} are effectively captured.

The strength of CP perturbation is quantified following Kirsch et al. (2021). The unperturbed states are defined as the medians within the 30-min window prior to t_0. The magnitudes of CP-induced perturbation are determined as the differences between the extreme values within 60 min after t_0 and the unperturbed states. For temperature, the extreme value is the minimum, while for pressure, relative humidity, and horizontal wind speed, it is the maximum. For specific humidity, the extreme values are determined by the sign of the 50-m value at 10 min after t_0 relative to the unperturbed state, which indicate either moistening (positive) or drying (negative) induced by CPs (e.g., Kirsch et al., 2021; Kruse et al., 2022). We also tested other time windows (5, 15, and 20 min) and found similar results. Additionally, the CP strength c is calculated using an equation that integrates temperature perturbations (ΔT) at all measurement levels from 10 m (z_0) to 350 m (z_t), and is linked to the theoretical CP speed (Rotunno et al., 1988; Grant and van den Heever, 2016):

$$c^2 = 2\int_{z_0}^{z_t} -g\frac{\Delta T}{T_{\text{env}}}\mathrm{d}z,$$

where T_{env} is the unperturbed environmental temperature, calculated as the median of the 30-min window prior to t_0, and g is the gravitational acceleration. Since this estimation tends to overestimate (or underestimate) the strength of CPs below (or above) 350 m when integrating ΔT at the measurement levels, the CP strength is used solely for qualitative comparison.

In addition, we analyze the CP depth, which is measured as the height where the temperature perturbation at 10 min after t_0 decreases to 0 K, based on the method outlined by Kruse et al. (2022). If no 0-K temperature anomalies are detected at the tower measurements levels, a linear extrapolation of the temperature is performed to estimate the CP height. Deviations of this estimation method are assessed against all CPs shallower than the tower, whose depth can be directly estimated with observation. The average deviation is 45 m, which is acceptable given the tower's vertical resolution (10–50-m intervals). Therefore, we believe this method is reasonable and practical.

2.3. *Classification of convection organizational modes*

To achieve better knowledge of the relationship between convective systems and CPs, CP events are grouped by the morphology of their parent convections, which are located closest to SZMT within the 30-min window prior to t_0. Following previous studies (Parker and Johnson, 2000; Schiro and Neelin, 2018), the parent convections are classified into three types: individual convective cells (CCs), linear MCSs (L-MCSs), and nonlinear MCSs (NL-MCSs). A convection is defined as the contiguous area with reflectivity ⩾ 30 dBZ. A CC is characterized by convection with its length smaller than 100 km in any direction. An MCS refers to convection with its length scale greater than 100 km. Following the MCS organizational mode classification method in South China (Li et al., 2021), an MCS with a length/width ratio of larger than 1.8 in an area with reflectivity ⩾ 40 dBZ is identified as an L-MCS, while those not meeting this criterion are categorized as NL-MCSs.

3. Cold pool features

3.1. *Seasonal and diurnal variations of CP occurrence*

A total of 164 CP events were recorded at SZMT during 2018–20, with significant seasonal variations (Figs. 2a and b). From May to June, during the pre-summer rainy season, the rain belt swings over South China due to the combined influences of synoptic systems in the westerlies and the summer monsoon flow (Ding, 1992). As the rainy season begins, CP occurrences begin to increase (Fig. 2a). CPs become active from June to September, accounting for 84.8% of all events, basically coinciding with the onset and subsequent retreat of the summer monsoon. Despite a reduction in rainfall during the summer monsoon retreat in September, CP occurrences remain active. This persistence is likely related to the relatively drier environmental conditions following the summer monsoon's retreat, which favors evaporation (Fig. 2b). Although precipitation begins to increase significantly in May due to the enhanced heat, moisture supply from the summer monsoon flow and sea breeze activity (Zhu et al., 2017), CPs remain inactive in May, which is distinct from patterns observed in other regions with good agreement between CP activities and rainfall (e.g., Garg et al., 2021; Joseph et al., 2021).

Diurnally, CP occurrences peak from noon to afternoon (1200–1700 LST, Fig. 2c), corresponding to the peak in afternoon precipitation. This suggests a link to afternoon thermal convections, consistent with the afternoon rainfall peak (e.g., Du and Rotunno, 2018; Chen, 2020), as well as the peak in convection initiation (Bai et al., 2020). Typically, a lag is expected between the precipitation and the CP formation by its cooling. However, the varying propagation speeds of convection and CPs obscure this lag, as seen in Fig. 2c, which depicts CP passages at the tower. Observational studies have noted a small gap between CP passages and precipitation (Chandra et al., 2018), or gap of about 30 min (Schiro and Neelin, 2018). Given the hourly resolution, such a short lag time may not be discernible, making the apparent alignment between CP events and precipitation rate/frequency reasonable.

In South China, thermal afternoon convection is predominantly driven by solar radiation heating and land–sea breezes (Zhu et al., 2017; Bai et al., 2020). The northward sea breeze strengthens after 1000 LST (Fig. 2d), promoting both precipitation and CP occurrences. After 1900 LST, as the northward sea breeze transitions to a southward land breeze, both precipitation and CP occurrences decrease. In May, rainfall predominantly increases at night rather than in the afternoon (Figs. 2a and d). Since thermal convective rainfall constitutes less of the overall rainfall in May, CP events do not show a significant increase (Fig. 2a). Convective cooling at night is generally weak and insufficient to meet the threshold of CP identification (with ΔT_{10m} must be less than −2 K within 20 min) in the relatively cooler nighttime environment. As a result, cooler ambient temperatures and

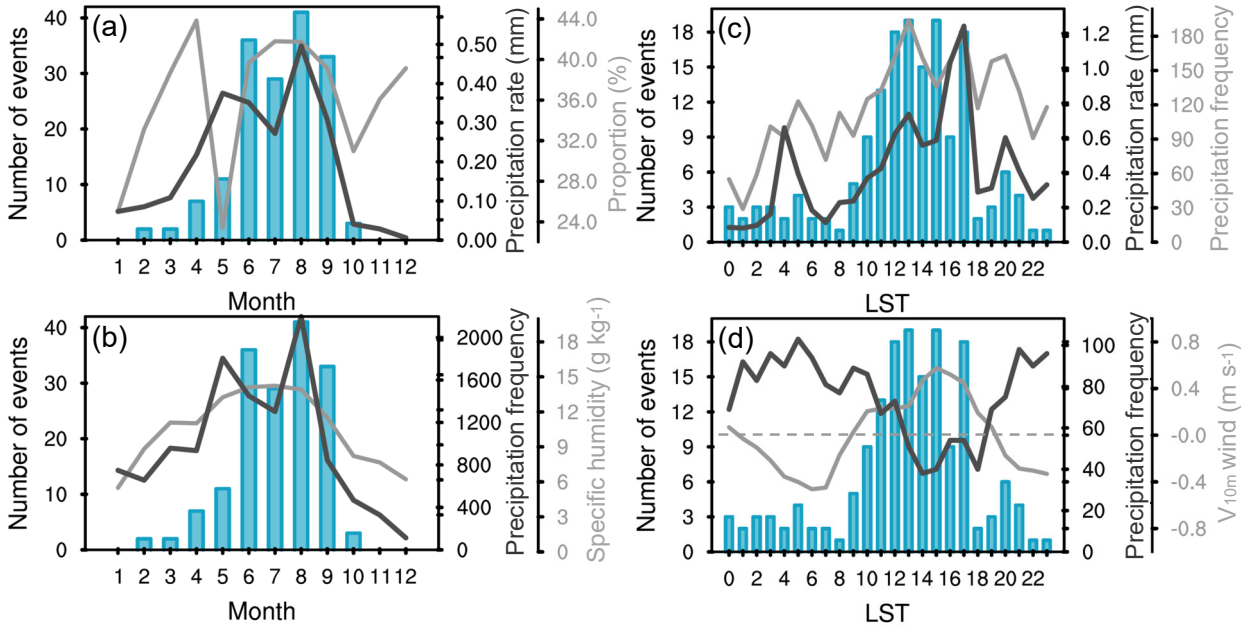

Fig. 2. Occurrence of CP events (bars) in (a, b) the annual cycle and (c, d) the diurnal cycle. Lines in (a) depict the precipitation rate (mm h^{-1}, black), the proportion of precipitation rate within 1200–2000 LST (%, gray), and in (b) the precipitation frequency (black line) and specific humidity (g kg^{-1}, gray) at 850 hPa. Specific humidity is averaged within a radius of 1° from SZMT of ECMWF atmospheric reanalysis (ERA5) data. The lines in (c) display the diurnal cycle of precipitation rate (black) and frequency (gray) on days with CP occurrences. The lines in (d) exhibit the diurnal cycle of the meridional component of wind perturbations at 10 m (m s^{-1}, gray) on days with CP occurrences, along with daily variations of precipitation frequency in May (black).

reduced rainfall suppress CP occurrence at night, with only 18.9% of total CP events observed between 2100 and 0700 LST.

These seasonal and diurnal variations emphasize the close relationship between CP occurrence and convective activity, consistent with findings in previous studies (e.g., Wang et al., 2014; Mai et al., 2023) and in other regions (e.g., Garg et al., 2021; Joseph et al., 2021), and highlight the influence of the summer monsoon and local forcing mechanisms in this area.

3.2. *Vertical structure*

The CP-related meteorological perturbations at various heights are shown in Figs. 3a–e. The passages of CPs cause a median temperature decrease of 3.68 K at 10 m and a median pressure increase of 0.40 hPa at 50 m. Cold and dense air within the CP tends to settle and accumulate near the ground, causing smaller perturbations at higher altitudes (e.g., a median decrease of 1.97 K in temperature at 350 m, and an increase of 0.20 hPa in pressure at 300 m). The denser air within the interior of CPs compared to the environment enhances horizontal winds at the CP edge (gust front), with an increase of 3.3 m s^{-1} at 10 m, and up to 4.7 m s^{-1} at 160 m, where surface friction is absent. Above 160 m, wind speed anomalies remain generally consistent. These near-surface signals are generally stronger than those of CPs in tropical oceanic conditions and weaker than those in midlatitude continental regions (Engerer et al., 2008; Terai and Wood, 2013; Chandra et al., 2018; Kirsch et al., 2021; Wills et al., 2021).

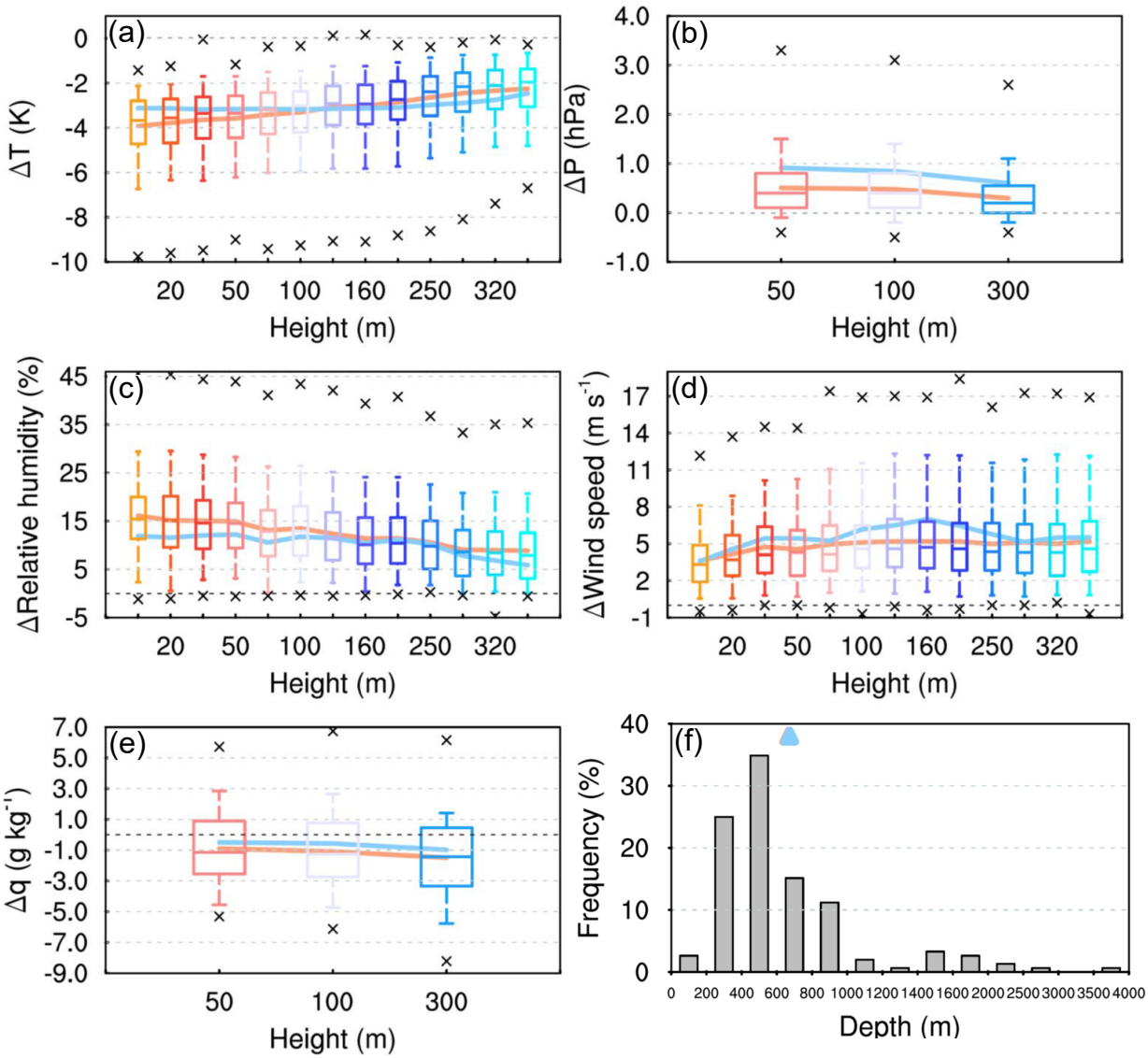

Fig. 3. Vertical distributions of perturbations in (a) temperature (K), (b) pressure (hPa), (c) relative humidity (%), (d) wind speed (m s^{-1}), and (e) specific humidity (g kg^{-1}), and (f) the frequency of CP depth (%). In panels (a–e), the horizontal line, box, and whiskers represent the median, inter-quartile range, and the 5th and 95th percentiles, respectively, while crosses denote extreme values. The colored thick lines and triangles represent the average value of CP events occurring during April–September (warm season, red) and October–March (cold season, blue).

Effects on specific humidity are analyzed separately due to the inconsistent signals observed in various climatic regimes (Feng et al., 2015; de Szoeke et al., 2017; Trzeciak et al., 2017; Schiro and Neelin, 2018; Kirsch et al., 2021). Following the judgement in section 2.2, only 35.37% of CPs increase the specific humidity, while 64.63% cause drops of moisture. The variability of humidity perturbation is linked to two competing processes related to CP formation: evaporation of raindrops moistens the atmosphere, and downward transport of dry air masses from mid-levels reduces the atmospheric humidity (Wood et al., 2011; Zuidema et al., 2012). In the moistening CP group, stronger evaporation outcompetes the drying of downward transport of mid-level air, causing increases in specific humidity, particularly near the surface because of the larger evaporation there (Fig. 3e). In the drying group, downward entrainment of dry air is the principal factor, with greater moisture reductions at higher levels. More CP passages (64.63%) are followed by a decrease in specific humidity, indicating the dominance of downward import of upper dry air masses in the formation of a large proportion of CPs in this region. This is probably related to the suppressed evaporation in the wet conditions. Generally, the CPs lead to a median decrease of 1.15 g kg^{-1} in specific humidity at 50 m and 1.42 g kg^{-1} at 300 m. This differs to a study over the continental midlatitudes, in which an average increase was observed and 64% of the variability in CP strength was attributed to evaporative cooling alone (Kirsch et al., 2021). Despite the reduction in specific humidity, the cooling in temperature results in an increase of 15.44% in relative humidity at 10 m, which diminishes to 7.87% at 350 m as the cooling weakens (Fig. 3c).

The depth of the CP is a critical parameter for subsequent convection triggering. In this study, most CPs have estimated depths of 200–400 m (25.0%) and 400–600 m (34.9%), with an average depth of 668.0 m and a maximum of 3640.7 m (Fig. 3f). When using the vertical temperature gradient after 5, 15, and 20 min of CP passages to estimate CP depth, comparable average depths of 616.9 m, 679.5 m, and 629.6 m are obtained, respectively. This is higher than the average of 300 m observed over tropical oceans (Terai and Wood, 2013; de Szoeke et al., 2017), but slightly lower than the depth of 746 m over continental Germany (Kirsch et al., 2021). A comparable CP depth of about 500 m has been inferred from a tower at a coastal region in the Netherlands (Kruse et al., 2022).

CP signals between warm and cold seasons are compared. CPs in the warm seasons exhibit features similar to all events. CPs during cold seasons produce larger pressure increases than those in warm seasons. However, perturbations of temperature and relative humidity are smaller in cold seasons due to weaker precipitation (Fig. 2a). Decreases in specific humidity in cold seasons are weaker since more CPs (57%) have a positive sign of specific humidity change, indicating moisture enhancement, which is probably related to the surpassing evaporation under the drier conditions. This corresponds to the increase in moisture after CP passages over dry soils found in the numerical study by Drager et al. (2020). Their study shows that dry soils lead to greater daytime surface heating, which produces drier conditions in the subcloud layer, ultimately resulting in more evaporative cooling. CPs during cold seasons have an average depth of 667.8 m, which is approximately the same as that during warm seasons (673.6 m). Perturbations in wind speed do not vary much between different seasons.

3.3. *Temporal evolution during CP passage*

Figure 4 displays the composite time series before and after CP passages. After CPs pass (t_0), the near-surface tem-

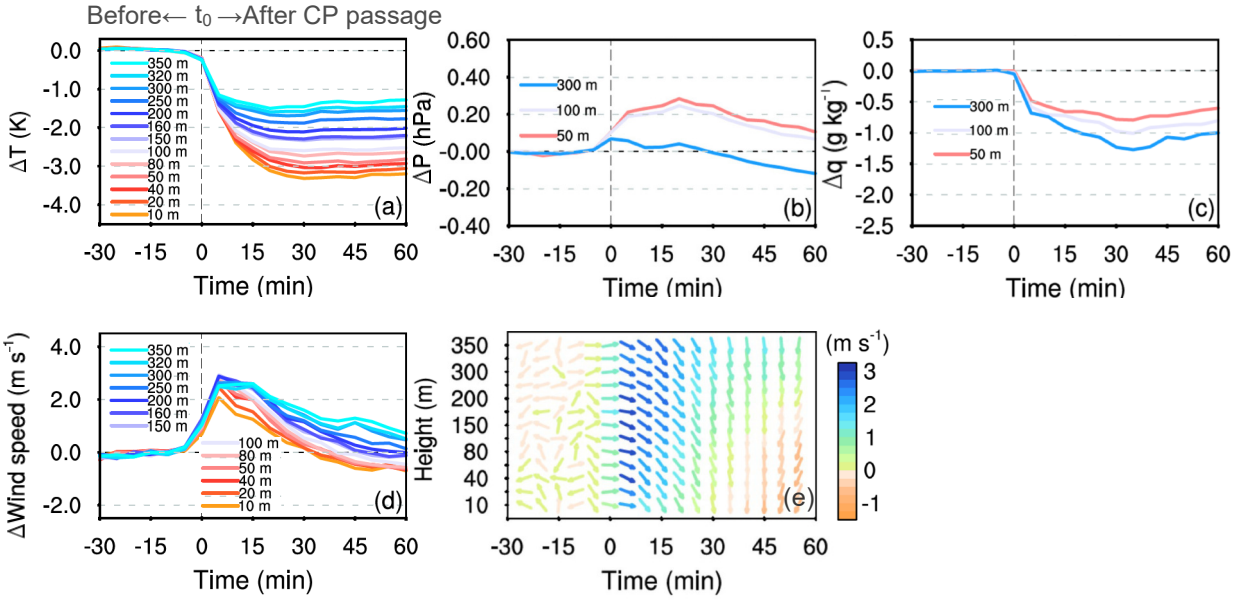

Fig. 4. Composite time series relative to the unperturbed state of (a) temperature (K), (b) pressure (hPa), (c) specific humidity (g kg^{-1}), (d) horizontal wind speed (m s^{-1}), and (e) horizontal wind field (m s^{-1}), respectively.

perature rapidly drops within 20 min and reaches its minimum around 30 min post-passage. Then, the near-surface temperature slowly recovers but remains lower than the pre-CP unperturbed state even one hour after t_0. This evolution is consistent with the findings from previous studies (e.g., Schiro and Neelin, 2018; Kruse et al., 2022). Pressure perturbations peak approximately 20 min after t_0. Compared with the sustained cooling, the pressure increases nearly recover one hour after t_0.

The composite of specific humidity decreases after t_0, indicating a dry interior of CPs (Fig. 4c). This dry interior is likely due to the suppression of evaporation and the significant contribution of the downward transport of mid-tropospheric dry air masses, as suggested in section 3.2. This feature is commonly observed in wet regimes, such as the West African Sahel during the monsoon season (Provod et al., 2016), tropical oceans (Chandra et al., 2018; Schiro and Neelin, 2018), and midlatitude coastal regions (Kruse et al., 2022). This contrasts with the results from the West African Sahel during the pre-monsoon period (Provod et al., 2016) and midlatitude continents (Kirsch et al., 2021), where the moistened interiors of CPs cause specific humidity increases. The variability in the humidity signal across various regimes aligns with results from simulation studies, which show the characteristics of CP interiors are distinct under various soil moisture conditions (Drager et al., 2020). Dry soil generates a dry subcloud layer, where a moist CP interior appears, whereas wetter soil conditions produce drier CP signals. The moist CP interior over dry soil results from significant hydrometeor evaporation within the CPs' parent rain shafts. In contrast, over the wet soil, a nearly hydrometeor-free downdraft originates from the cloud base, generating a larger negative surface moisture perturbation.

The drops in specific humidity imply the absence of evident moisture rings at CPs' leading edges, unlike those over tropical oceans. This difference might be due to the smaller magnitude of latent heat fluxes over land (Chandra et al., 2018; Drager et al., 2020; Kruse et al., 2022). The specific humidity keeps decreasing until about 35 min after t_0, and then gradually recovers.

A gust front, generated by the enhanced pressure gradient, forms at the CP edge, with the maximum signals of 10-m wind appearing within the first 5 min (Fig. 4d). The strongest winds below 160 m occur 5 min after t_0, while winds above 160 m reach their peak 10 min later. This timing window corresponds to the length of the CP nose (Goff, 1976; Kruse et al., 2022). Winds near the surface recover around 30 min after t_0, while winds at higher altitudes take more than one hour to fully revert to the unperturbed state. The wind anomalies associated with the gust front are primarily westerlies (Fig. 4e). Gust fronts vary in directions and intensity at different portions of a CP. However, they are typically strongest in the direction of the parent convection's propagation. The prevailing westerlies suggest that eastward-moving convective systems are the most common producers of CPs in this region. Behind the gust front, the drag of cold-air outflow caused by the surface friction induces a backflow of cold air near the surface (Goff, 1976). As a result, the near-surface winds rotate clockwise from westerlies to northeasterlies, indicating the passages of backflow behind the gust front. The sharp gradients in temperature, pressure, humidity, and wind speed at the CP edge suggest a boundary conducive to convection initiation. Time series of CP passages in the warm season exhibit features similar to all events, while CPs in the cold seasons show a more gradual evolution.

3.4. *Cold pools related to different convection modes*

According to the identification in section 2.3, 50.3% of CPs are related to CCs. At nighttime (1800–0800 LST), more CPs are produced by MCSs (55.6%). A greater proportion of daytime CPs (0900–1700 LST) are generated by CCs (66.7%). On average, CPs generated by CCs are shallower, with an average depth of 595.8 m, while those by MCSs are deeper, with 770.5 m for L-MCSs and 733.4 m for NL-MCSs (Fig. 5a). Correspondingly, CPs produced by MCSs are stronger, and L-MCS-related CPs exhibit the greatest strength (Fig. 5b).

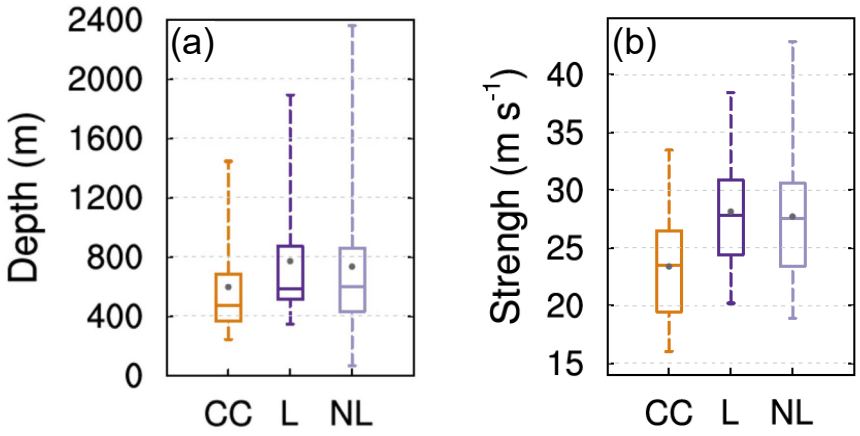

Fig. 5. Distributions of (a) CP depth (m) and (b) strength (m s^{-1}) for different convection modes. Dots denote average values.

Overall, the CPs generated by MCSs demonstrate stronger perturbations and larger gradients of all measured variables at each level (Fig. 6). Furthermore, the specific humidity affected by CC-related CPs slightly increases at 50 m within 10 min of t_0, which is similarly presented in Chandra et al. (2018) (Fig. 6g). Gust fronts produced by different types of convections exhibit various directions, with southeasterlies for CC-related CPs, northwesterlies for L-MCS-related CPs, and westerlies for NL-MCS-related CPs (Figs. 6m–o). This suggests that the typical movement direction of each type of convection varies, which is influenced by the background environmental flows. For instance, CCs often occur in the afternoon when a southeasterly sea breeze drives convection northwestward. For MCSs, which can develop more deeply, they are affected by the westerlies and principally move eastward. After NL-MCS-related CPs pass, it takes longer (~45 min) for the temperature and humidity to reach their minimums, and for the winds to recover. This period is shorter for L-MCS-related CPs (~25 min). Since CPs from two types of MCSs result in comparable magnitudes of wind perturbations (Figs. 6k–l), it can be inferred that these CPs have similar propagation speeds (Goff,

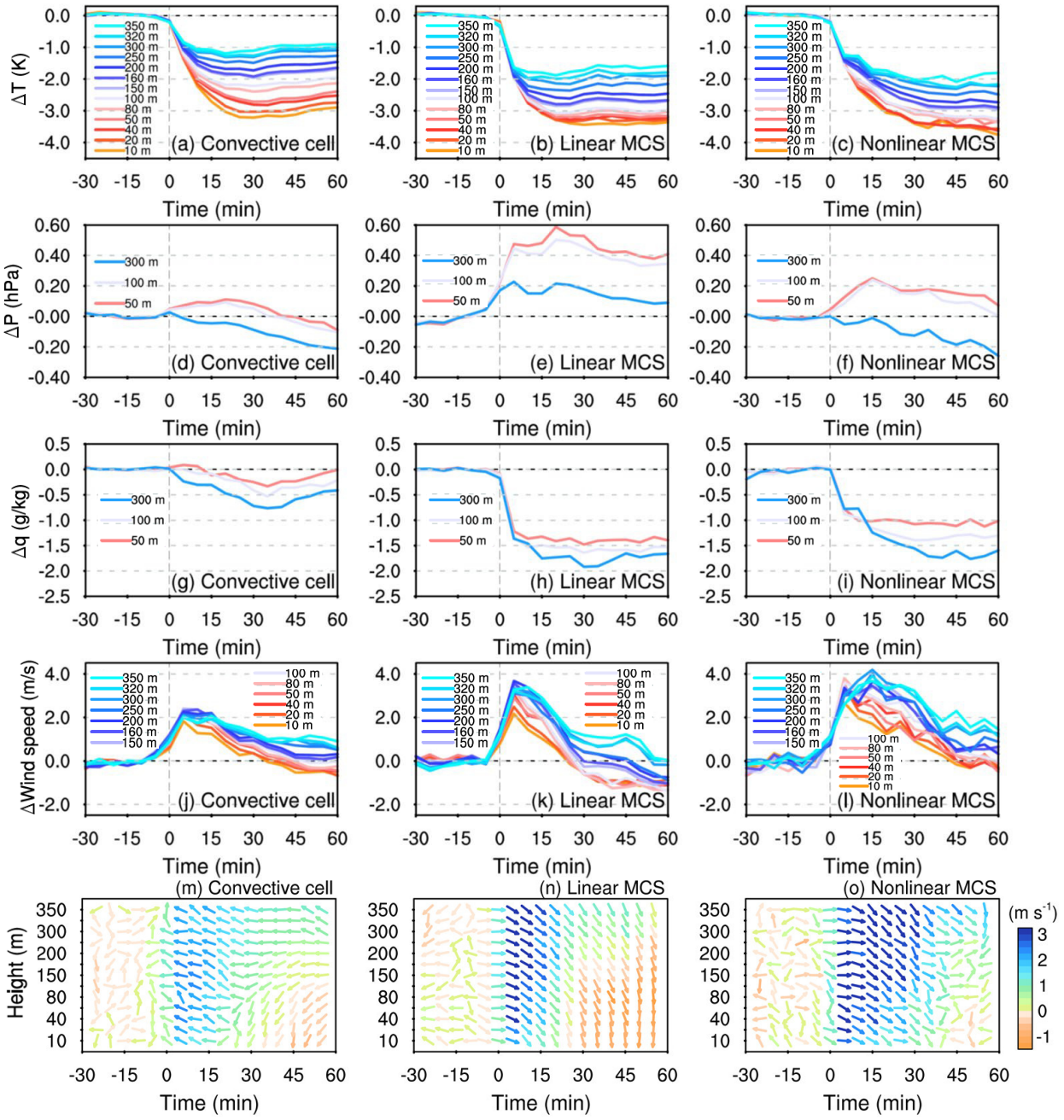

Fig. 6. Composite time series of variables relative to the unperturbed state for CPs related to different convection modes. The left list is for CC type, the middle list for L-MCS type, and the right list for NL-MCS type. Variables of (a–c) temperature (K), (d–f) pressure (hPa), (g–i) specific humidity (g kg^{-1}), (j–l) horizontal wind speed (m s^{-1}), and (m–o) horizontal wind field (m s^{-1}).

1976). Therefore, the long duration of signals related to NL-MCSs suggests a greater length in the directions of MCS propagation compared to L-MCS-related CPs.

3.5. *CP signals in the diurnal cycle*

Figure 7 illustrates the diurnal variations of CP signals. The most intense signals of pressure and wind speed in the diurnal cycle exhibit a primary peak at night (2000–2300 LST) and a secondary peak in the early morning (0400–0700 LST) (Fig. 7a). Conversely, pressure and wind perturbations are relatively weak in the middle of the night (0000–0300 LST) and in the afternoon (1200–1500 LST). The composite of specific humidity perturbation shows a reduction compared to the unperturbed value throughout the day (Fig. 7b), with a similar bimodal pattern, with the primary peak at night (2000–2300 LST), a minor peak in the early morning (0400–0700 LST), and a minimum in the afternoon (1200–1500 LST).

Most measured variables have similar diurnal patterns across all levels. However, temperature deficits at the near-

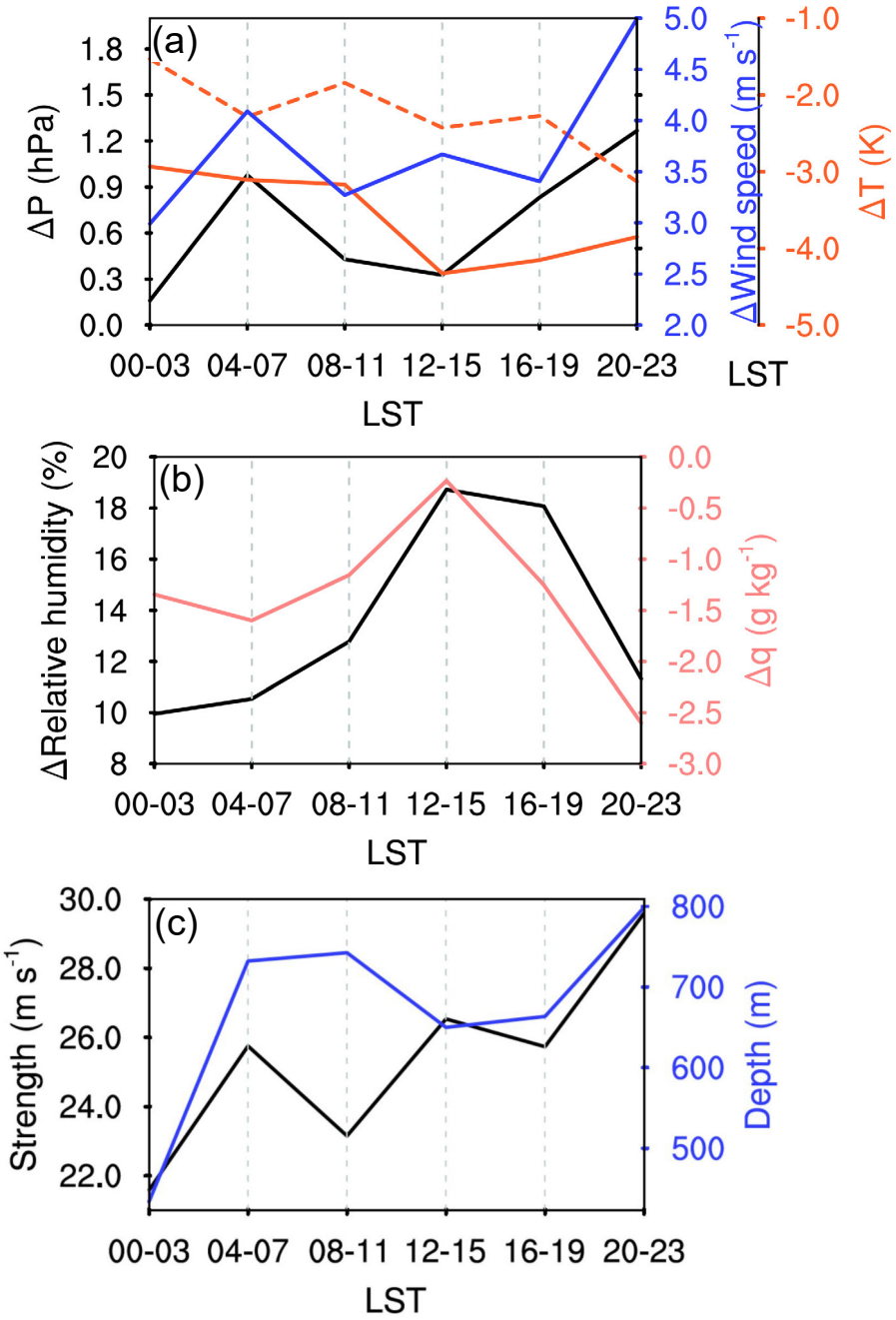

Fig. 7. Diurnal variations of averaged perturbations in (a) pressure at 50 m (hPa), wind speed at 10 m (m s^{-1}), temperature (K) at 10 m (solid) and 350 m (dashed), (b) relative humidity at 10 m (%) and specific humidity at 50 m (g kg^{-1}), and (c) averaged CP strength (m s^{-1}) and depth (m).

surface levels and higher levels show different diurnal variations. The maximum temperature perturbation at 10 m is observed at 1200–1500 LST, while at 350 m, it occurs at 2000–2300 LST (Fig. 7a). When calculating the CP strength with the integrated anomalies, CPs have peaks near 2000–2300 LST and 0400–0700 LST in depth and strength (Fig. 7c), indicating that more cold air masses deposit within these CPs. This results in more notable increases in pressure and smaller vertical gradients of temperature perturbations, with temperature deficits at high levels remaining large and thus able to dissipate at higher altitudes. This suggests a deeper CP depth, corresponding to the larger depths of 798.6 m and 732.2 m at 2000–2300 LST and 0400–0700 LST. CPs occurring at 1200–1500 LST are shallower (650.0 m), producing weaker perturbations in pressure and larger vertical gradients in temperature changes, which shows a large discrepancy between cooling at low and high levels. The cooling therefore decays at low altitudes. Numerical studies also emphasize varying CP intensity variations when considering the near-surface cooling and the integrated buoyancy, highlighting the necessity for detailed observations of the vertical structure of CPs (Grant and van den Heever, 2016).

The L-MCS-related CPs dominate at night (2000–2300 LST) and in the morning (0400–0700 LST) (Fig. 8). As shown in section 3.4, L-MCSs produce the strongest and deepest CPs. This is consistent with the diurnal cycle in which stronger and deeper CPs cause larger perturbations in the corresponding period (Fig. 7). At 0000–0300 LST and 1200–1500 LST, when CPs are more frequently associated with CCs, they tend to generate shallower CPs causing weaker anomalies (Figs. 5 and 6). Thus, CPs during these hours are shallower, leading to weaker perturbations.

4. Summary and discussion

This study utilizes observational data from SZMT, collected during 2018–20, to analyze the characteristics of CPs in a coastal monsoon region of South China. CPs mainly occur after the onset of summer monsoon (June–September), and exhibit a pronounced diurnal cycle, with high frequency in the afternoon (1200–1700 LST). The occurrence of CPs is closely linked to convective systems influenced by the summer monsoon and land–sea breeze activities, which modulate their seasonal and diurnal patterns, respectively. The wet conditions driven by the summer monsoon also modify the CP occurrences.

The tower observations provide insights into the vertical variations of CP properties, capturing signals in the near-surface boundary layer. The passage of a CP causes a pronounced temperature decrease, rise in pressure, and increasing in relative humidity at lower levels, as well as distinct acceleration of winds below 160 m. The magnitudes of these perturbations are generally intermediate between those observed in tropical and midlatitude regions (e.g., Engerer et al., 2008; Terai and Wood, 2013; Wills et al., 2021). CPs can either increase or decrease the specific humidity in the boundary layer, with stronger moistening near the surface or greater drying at higher altitudes. Of the observed CPs, 64.63% feature a dry interior in specific humidity, similar to the structure observed under wetter conditions (e.g., Provod et al., 2016; Chandra et al., 2018; Schiro and Neelin, 2018). This suggests that the transport of dry air through convective downdrafts is a primary process in CP formation, surpassing the effects of the suppressed evaporation within the humid monsoon-influenced climate. The average CP depth is estimated at 668.0 m, which is deeper than tropical oceanic CPs yet shallower than those in midlatitude continental regions (Terai and Wood, 2013; Kirsch et al., 2021).

Distinct CP structures, including the CP nose, backflow, and gust front, are identified by the tower. Moisture rings near the CP edge are less common compared to those in tropical ocean areas, likely due to the smaller magnitude of latent heat fluxes over land (Drager et al., 2020; Kruse et al., 2022). The absence of moisture rings suggests an important role played by mechanical lifting in CPs for convection initiations, while their thermodynamic forcing appears less significant. Sharp gradients in temperature, pressure, and

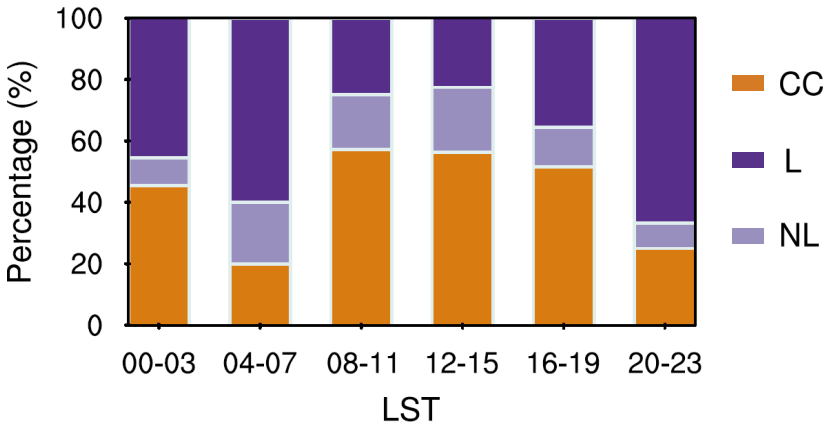

Fig. 8. Diurnal cycle of the percentage of parent convection modes producing CPs.

wind speed at the CP edge foster convergence, triggering new convection activities.

CPs associated with MCSs are generally stronger and deeper, yielding more intense signals than those from individual CCs. L-MCSs produce the strongest and deepest CPs. With high occurrence of L-MCS-type CPs at night (2000–2300 LST) and in the early morning (0400–0700 LST), signals of CPs and their depth and strength peak at these two times in the diurnal cycle. CPs related to NL-MCSs exhibit a longer duration, attributable to the longer length of the MCS in its propagation direction. The directions of outflow anomalies vary across diverse convection modes, revealing the different typical movement directions for each mode, which are driven by varying background wind flows.

This study underscores that CPs exhibit varied structures across different convective modes and large-scale weather conditions, leading to various effects or interactions with complex local factors that impact subsequent development and organization (e.g., Peters and Schumacher, 2015; Du et al., 2020). These findings highlight the need for further investigation into CP properties under varying synoptic conditions to clarify the complex relationships between heavy rainfall and the CPs they initiate. Such research will also contribute to improving the parameterization of CPs and the prediction of coastal precipitation events in numerical simulations.

Acknowledgements. This study was supported by the National Key Research and Development Program of China (Grant No. 2024YFC3013003), the National Natural Science Foundation of China (Grant No. 42475002), the Innovation Group Project of Southern Marine Science and Engineering Guangdong Laboratory (Zhuhai) (Grant Nos. SML2024SP035, SML2024SP012, and 311024001), the Guangdong Basic and Applied Basic Research Foundation (Grant Nos. 2025A1515011974, 2024A1515510005 and 2020B0301030004), and the Key Innovation Team of China Meteorological Administration (Grant No. CMA2023ZD08). We acknowledge the high-performance computing support from the School of Atmospheric Science of Sun Yat-sen University.

Data availability statement. The observational data from radar (https://data.cma.cn/data/cdcdetail/dataCode/J.0019.0010.S001.html) and in situ surface stations (https://data.cma.cn/data/cdcdetail/dataCode/A.0013.0001.html) can be obtained from the National Meteorological Information Center of the China Meteorological Administration. ERA5 data are available from https://www.ecmwf.int/en/forecasts/dataset/ecmwf-reanalysis-v5. The tower data of cold pool events are uploaded at https://github.com/ChuyMai/SZMT_cpevents.

REFERENCES

Bai, L. Q., G. X. Chen, and L. Huang, 2020: Convection initiation in monsoon coastal areas (South China). *Geophys. Res. Lett.*, **47**, e2020GL087035, https://doi.org/10.1029/2020GL087035.

Böing, S. J., H. J. J. Jonker, A. P. Siebesma, and W. W. Grabowski, 2012: Influence of the subcloud layer on the development of a deep convective ensemble. *J. Atmos. Sci.*, **69**(9), 2682–2698, https://doi.org/10.1175/JAS-D-11-0317.1.

Chandra, A. S., P. Zuidema, S. Krueger, A. Kochanski, S. P. de Szoeke, and J. H. Zhang, 2018: Moisture distributions in tropical cold pools from equatorial Indian Ocean observations and cloud-resolving simulations. *J. Geophys. Res.*, **123**, 11 445–11 465, https://doi.org/10.1029/2018JD028634.

Chen, G. X., 2020: Diurnal cycle of the Asian summer monsoon: Air pump of the second kind. *J. Climate*, **33**(5), 1747–1775, https://doi.org/10.1175/JCLI-D-19-0210.1.

de Szoeke, S. P., E. D. Skyllingstad, P. Zuidema, and A. S. Chandra, 2017: Cold pools and their influence on the tropical marine boundary layer. *J. Atmos. Sci.*, **74**(4), 1149–1168, https://doi.org/10.1175/JAS-D-16-0264.1.

Ding, Y. H., 1992: Summer monsoon rainfalls in China. *J. Meteor. Soc. Japan*, **70**(1B), 373–396, https://doi.org/10.2151/jmsj1965.70.1B_373.

Drager, A. J., L. D. Grant, and S. C. van den Heever, 2020: Cold pool responses to changes in soil moisture. *Journal of Advances in Modeling Earth Systems*, **12**(8), e2019MS001922, https://doi.org/10.1029/2019MS001922.

Du, Y., and R. Rotunno, 2018: Diurnal cycle of rainfall and winds near the south coast of China. *J. Atmos. Sci.*, **75**(6), 2065–2082, https://doi.org/10.1175/JAS-D-17-0397.1.

Du, Y., G. X. Chen, B. Han, L. Q. Bai, and M. H. Li, 2020: Convection initiation and growth at the coast of South China. Part II: Effects of the terrain, coastline, and cold pools. *Mon. Wea. Rev.*, **148**(9), 3871–3892, https://doi.org/10.1175/MWR-D-20-0090.1.

Engerer, N. A., D. J. Stensrud, and M. C. Coniglio, 2008: Surface characteristics of observed cold pools. *Mon. Wea. Rev.*, **136**(12), 4839–4849, https://doi.org/10.1175/2008MWR2528.1.

Feng, Z., S. Hagos, A. K. Rowe, C. D. Burleyson, M. N. Martini, and S. P. de Szoeke, 2015: Mechanisms of convective cloud organization by cold pools over tropical warm ocean during the AMIE/DYNAMO field campaign. *Journal of Advances in Modeling Earth Systems*, **7**(2), 357–381, https://doi.org/10.1002/2014MS000384.

Garcia-Carreras, L., and Coauthors, 2013: The impact of convective cold pool outflows on model biases in the Sahara. *Geophys. Res. Lett.*, **40**, 1647–1652, https://doi.org/10.1002/grl.50239.

Garg, P., S. W. Nesbitt, T. J. Lang, and G. Priftis, 2021: Diurnal cycle of tropical oceanic mesoscale cold pools. *J. Climate*, **34**(23), 9305–9326, https://doi.org/10.1175/JCLI-D-20-0909.1.

Goff, R. C., 1976: Vertical structure of thunderstorm outflows. *Mon. Wea. Rev.*, **104**, 1429–1440, https://doi.org/10.1175/1520-0493(1976)104<1429:VSOTO>2.0.CO;2.

Grant, L. D., and S. C. van den Heever, 2016: Cold pool dissipation. *J. Geophys. Res.*, **121**(3), 1138–1155, https://doi.org/10.1002/2015JD023813.

Joseph, J., M. S. Girishkumar, M. J. McPhaden, and E. P. R. Rao, 2021: Diurnal variability of atmospheric cold pool events and associated air-sea interactions in the Bay of Bengal during the summer monsoon. *Climate Dyn.*, **56**(3), 837–853, https://doi.org/10.1007/s00382-020-05506-w.

Kirsch, B., F. Ament, and C. Hohenegger, 2021: Convective cold pools in long-term boundary layer mast observations. *Mon. Wea. Rev.*, **149**(3), 811–820, https://doi.org/10.1175/MWR-D-20-0197.1.

Kruse, I. L., J. O. Haerter, and B. Meyer, 2022: Cold pools over the Netherlands: A statistical study from tower and radar observations. *Quart. J. Roy. Meteor. Soc.*, **148**(743), 711–726, https://doi.org/10.1002/qj.4223.

Li, S., Z. Y. Meng, and N. G. Wu, 2021: A preliminary study on the organizational modes of mesoscale convective systems associated with warm-sector heavy rainfall in South China. *J. Geophys. Res.*, **126**, e2021JD034587, https://doi.org/10.1029/2021JD034587.

Liu, X., Y. L. Luo, Z. Y. Guan, and D.-L. Zhang, 2018: An extreme rainfall event in coastal south China during SCMREX‐2014: Formation and roles of rainband and echo trainings. *J. Geophys. Res.*, **123**(17), 9256–9278, https://doi.org/10.1029/2018JD028418.

Mai, C. Y., Y. Du, and M. H. Li, 2023: Processes of colliding cold pools derived from a 356-m-high Shenzhen met-tower during an extremely heavy rainfall event. *Mon. Wea. Rev.*, **151**, 1571–1585, https://doi.org/10.1175/MWR-D-22-0214.1.

Marion, G. R., and R. J. Trapp, 2019: The dynamical coupling of convective updrafts, downdrafts, and cold pools in simulated supercell thunderstorms. *J. Geophys. Res.*, **124**(2), 664–683, https://doi.org/10.1029/2018JD029055.

Markowski, P., and Y. Richardson, 2010: *Mesoscale Meteorology in Midlatitudes*. Wiley-Blackwell, 407 pp.

Meyer, B., and J. O. Haerter, 2020: Mechanical forcing of convection by cold pools: Collisions and energy scaling. *Journal of Advances in Modeling Earth Systems*, **12**, e2020MS002281, https://doi.org/10.1029/2020MS002281.

Parker, M. D., and R. H. Johnson, 2000: Organizational modes of midlatitude mesoscale convective systems. *Mon. Wea. Rev.*, **128**(10), 3413–3436, https://doi.org/10.1175/1520-0493(2001)129<3413:OMOMMC>2.0.CO;2.

Peters, J. M., and R. S. Schumacher, 2015: Mechanisms for organization and echo training in a flash-flood-producing mesoscale convective system. *Mon. Wea. Rev.*, **143**, 1058–1085, https://doi.org/10.1175/MWR-D-14-00070.1.

Provod, M., J. H. Marsham, D. J. Parker, and C. E. Birch, 2016: A characterization of cold pools in the West African Sahel. *Mon. Wea. Rev.*, **144**(5), 1923–1934, https://doi.org/10.1175/MWR-D-15-0023.1.

Rotunno, R., J. B. Klemp, and M. L. Weisman, 1988: A theory for strong, long-lived squall lines. *J. Atmos. Sci.*, **45**(3), 463–485, https://doi.org/10.1175/1520-0469(1988)045<0463:ATFSLL>2.0.CO;2.

Schiro, K. A., and J. D. Neelin, 2018: Tropical continental downdraft characteristics: Mesoscale systems versus unorganized convection. *Atmospheric Chemistry and Physics*, **18**(3), 1997–2010, https://doi.org/10.5194/acp-18-1997-2018.

Su, L., X. Sun, Y. Du, J. C. H. Fung, and G. X. Chen, 2023: The roles of local convergences in the convection initiation of a record-breaking rainfall event at the coastal Pearl River Delta in South China. *J. Geophys. Res.*, **128**, e2022JD037234, https://doi.org/10.1029/2022JD037234.

Terai, C. R., and R. Wood, 2013: Aircraft observations of cold pools under marine stratocumulus. *Atmospheric Chemistry and Physics*, **13**(19), 9899–9914, https://doi.org/10.5194/acp-13-9899-2013.

Tompkins, A. M., 2001: Organization of tropical convection in low vertical wind shears: The role of cold pools. *J. Atmos. Sci.*, **58**, 1650–1672, https://doi.org/10.1175/1520-0469(2001)058<1650:OOTCIL>2.0.CO;2.

Torri, G., and Z. M. Kuang, 2016: Rain evaporation and moist patches in tropical boundary layers. *Geophys. Res. Lett.*, **43**, 9895–9902, https://doi.org/10.1002/2016GL070893.

Torri, G., Z. M. Kuang, and Y. Tian, 2015: Mechanisms for convection triggering by cold pools. *Geophys. Res. Lett.*, **42**(6), 1943–1950, https://doi.org/10.1002/2015GL063227.

Trzeciak, T. M., L. Garcia-Carreras, and J. H. Marsham, 2017: Cross-Saharan transport of water vapor via recycled cold pool outflows from moist convection. *Geophys. Res. Lett.*, **44**, 1554–1563, https://doi.org/10.1002/2016GL072108.

van den Heever, S. C., and Coauthors, 2021: The Colorado state university convective CLoud outflows and UpDrafts experiment (C^3LOUD-Ex). *Bull. Amer. Meteor. Soc.*, **102**(7), E1283–E1305, https://doi.org/10.1175/BAMS-D-19-0013.1.

Wakimoto, R. M., 1982: The life cycle of thunderstorm gust fronts as viewed with Doppler radar and rawinsonde data. *Mon. Wea. Rev.*, **110**(8), 1060–1082, https://doi.org/10.1175/1520-0493(1982)110<1060:TLCOTG>2.0.CO;2.

Wang, H., Y. L. Luo, and B. J. -D. Jou, 2014: Initiation, maintenance, and properties of convection in an extreme rainfall event during SCMREX: Observational analysis. *J. Geophys. Res.*, **119**, 13 206–13 232, https://doi.org/10.1002/2014JD022339.

Wills, S. M., M. F. Cronin, and D. X. Zhang, 2021: Cold pools observed by uncrewed surface vehicles in the central and eastern tropical Pacific. *Geophys. Res. Lett.*, **48**, e2021GL093373, https://doi.org/10.1029/2021GL093373.

Wood, R., C. S. Bretherton, D. Leon, A. D. Clarke, P. Zuidema, G. Allen, and H. Coe, 2011: An aircraft case study of the spatial transition from closed to open mesoscale cellular convection over the Southeast Pacific. *Atmospheric Chemistry and Physics*, **11**(5), 2341–2370, https://doi.org/10.5194/acp-11-2341-2011.

Zhang, S. J., Z. M. Liang, D. H. Wang, and G. X. Chen, 2022: Nocturnal convection initiation over inland South China during a record-breaking heavy rainfall event. *Mon. Wea. Rev.*, **150**(11), 2935–2957, https://doi.org/10.1175/MWR-D-21-0264.1.

Zhu, L., Z. Y. Meng, F. Q. Zhang, and P. M. Markowski, 2017: The influence of sea‐ and land‐breeze circulations on the diurnal variability in precipitation over a tropical island. *Atmospheric Chemistry and Physics*, **17**, 13 213–13 232, https://doi.org/10.5194/acp-17-13213-2017.

Zuidema, P., and Coauthors, 2012: On trade wind cumulus cold pools. *J. Atmos. Sci.*, **69**(1), 258–280, https://doi.org/10.1175/JAS-D-11-0143.1.